Dynamically forming $Cu_3Mo_2O_9$/Cu heterojunction for efficient nitrate reduction in Zn-nitrate batteries

Jiaqi Ni[1], Jing Yan[1], Ying Tao[1], Jie Ding[2], Auttaphon Chachvalvutikul[3], Ouardia Akdim[3], Lingyue Liu[4], Shanshan Huang[1], Weixu Wang[1], Hongli Sun[1], Haifeng Qi[3,*], Chenliang Su[1,*] and Bin Liu[2,5*]

[1]International Collaboration Laboratory of 2D Materials for Optoelectronics Science and Technology of Ministry of Education, Institute of Microscale Optoelectronics, Shenzhen University, Shenzhen 518060, China

[2]Department of Materials Science and Engineering, City University of Hong Kong, Hong Kong SAR 999077, China

[3]Max Planck-Cardiff Centre on the Fundamentals of Heterogeneous Catalysis FUNCAT, Cardiff Catalysis Institute, School of Chemistry, Cardiff University, Cardiff CF10 3AT, United Kingdom

[4]Department of Applied Biology and Chemical Technology, The Hong Kong Polytechnic University, Hong Kong SAR 100872, China

[5]Department of Chemistry, Hong Kong Institute for Clean Energy (HKICE) & Center of Super-Diamond and Advanced Films (COSDAF), City University of Hong Kong, Hong Kong SAR 999077, China

[*]Corresponding author: qih11@cardiff.ac.uk (H. Qi), chmsuc@szu.edu.cn (C. Su) and bliu48@cityu.edu.hk (B. Liu)

Abstract

The sustainable production of ammonia (NH_3) via electrochemical nitrate reduction reaction (NO_3^- RR) presents a dual solution for environmental remediation and renewable energy storage. However, this process is hindered by the sluggish kinetics of sequential deoxygenation and hydrogenation steps, particularly under alkaline conditions where proton scarcity exacerbates competing hydrogen evolution reaction (HER). In this work, a heterostructured $Cu_3Mo_2O_9$/Cu is purposely designed that can be reductively formed during the NO_3^-RR to incorporate the advantages of dual-function active sites in the processes of water dissociation and nitrate reduction. Experimental and theoretical results indicate that the *in-situ* generated $Cu_3Mo_2O_9$ is proposed to facilitate H_2O dissociation and likely contribute to protons (H^+) supply, while the metallic Cu enhances nitrate adsorption and facilitates the subsequent deoxygenation. The $Cu_3Mo_2O_9$/Cu catalyst achieves an excellent NH_3 Faradaic efficiency (FE) of 97.5% at -0.5 V vs. RHE with an NH_3 yield rate of 19.3 mg h^{-1} mg_{cat}^{-1} in 0.05 M KNO_3. This performance is among the highest under neutral/alkaline H-cell conditions. The $Cu_3Mo_2O_9$/Cu based Zn-nitrate battery delivers a peak power density of 20.24 mW cm^{-2} and maintains an FE_{NH_3} of 93.8% at 60 mA cm^{-2}. This work not only elucidates the dynamic synergy of heterostructured catalysts for multi-step reactions but also establishes a general framework for coupling catalytic nitrate conversion with energy storage applications.

Introduction

The electrochemical reduction of nitrate (NO_3^-) to ammonia (NH_3) presents a dual benefit by mitigating nitrate pollution while providing a sustainable route to carbon-free fertilizers.[1-3] Among emerging strategies, Zn-nitrate battery offers a promising approach by integrating energy storage with NO_3^--to-NH_3 conversion, addressing both environmental and energy challenges.[4-6] However, the practical implementation of Zn-nitrate battery is hindered by the sluggish kinetics of the nitrate reduction reaction (NO_3^-RR), a complex eight-electron transfer reaction involving sequential deoxygenation ($*NO_3^- \rightarrow *NO_2^- \rightarrow *NO$) and hydrogenation ($*NO \rightarrow *NH_3$) steps.[7,8] Critically, the hydrogenation of nitrate ($*NO_3^- \rightarrow *NH_3$) is the rate-determining step (RDS), due to the high energy barrier associated with N–O bond cleavage (204 kJ mol^{-1}) and the limited proton (H^+) availability in neutral or alkaline electrolytes (pH ≥ 7).[9-11] Conventional monometallic catalysts, such as Cu-based catalysts, often struggle to efficiently activate NO_3^- and dissociate water ($H_2O \rightarrow H^+ + OH^-$)

simultaneously.[12,13] This imbalance results in low Faradaic efficiency (FE) and poor selectivity in NO_3^- RR, which is caused by the competition with the hydrogen evolution reaction (HER).[14,15]

To achieve efficient NO_3^-RR to ammonia, catalyst design must strategically decouple these two steps: optimizing NO_3^- adsorption at one active site while promoting H_2O dissociation at the another.[16-18] Especially the interfacial H_2O plays a crucial role in governing proton supply, hydrogen bonding, and intermediate stabilization during electrochemical nitrate reduction; the interfacial H_2O orientation, and the hydrogen-bond network reorganization could impact on proton-coupled electron transfer.[19-21]Interfacial engineering of heterostructured catalysts has emerged as a promising strategy to achieve this spatial separation, enabling precise control over electronic structures and intermediate adsorption energies.[22-24] For instance, heterojunction with asymmetric charge redistribution can modulate the d-band center of active sites, accelerating both deoxygenation and hydrogenation kinetics. However, most reported heterostructures suffer from static interfacial interactions, limiting their structural adaptability under operational conditions.[25,26] Additionally, achieving well-defined spatial separation of active sites for step-specific catalysis remains a major challenge, necessitating further advancements in rational catalyst design.

Herein, we present a dynamically evolving $Cu_3Mo_2O_9$/CuO catalyst that is able to *in-situ* reconstruct into a $Cu_3Mo_2O_9$/Cu heterostructure during NO_3^-RR. This architecture uniquely integrates two functional components: (1) the $Cu_3Mo_2O_9$ phase with stable Mo sites that are proposed to facilitate H_2O dissociation and likely contribute to proton supply under reaction conditions, and (2) the metallic Cu phase, derived from selective reduction of CuO, which promotes NO_3^- adsorption and facilitates deoxygenation. *Operando* Raman spectroscopy and cyclic voltammetry measurements confirm the structural evolution of CuO to metallic Cu while preserving $Cu_3Mo_2O_9$ during NO_3^-RR. *In-situ* attenuated total reflectance surface-enhanced infrared spectroscopy (ATR-SEIRAS) measurements and density functional theory (DFT) calculations reveal that the heterointerface of $Cu_3Mo_2O_9$ and Cu in $Cu_3Mo_2O_9$/Cu optimizes $*NO_2^-$ adsorption energy and accelerates interfacial proton transfer. Consequently, the *in-situ* generated $Cu_3Mo_2O_9$/Cu catalyst achieves an excellent FE_{NH_3} of 97.5% at -0.5 V *vs.* RHE with an NH_3 yield rate of 19.3 mg h^{-1} mg_{cat}^{-1}, which is among the highest reported values under neutral/alkaline conditions. Furthermore, the Zn-nitrate battery assembled using $Cu_3Mo_2O_9$/Cu delivers a peak power density of 20.24 mW cm^{-2} with an FE_{NH_3} of 93.8%, demonstrating promising application for simultaneous energy storage and wastewater remediation. This work

advances the rational design of adaptive heterostructured catalysts for multi-step reactions, offering a universal framework to engineer spatially decoupled active sites in electrocatalysis.

Results and discussion

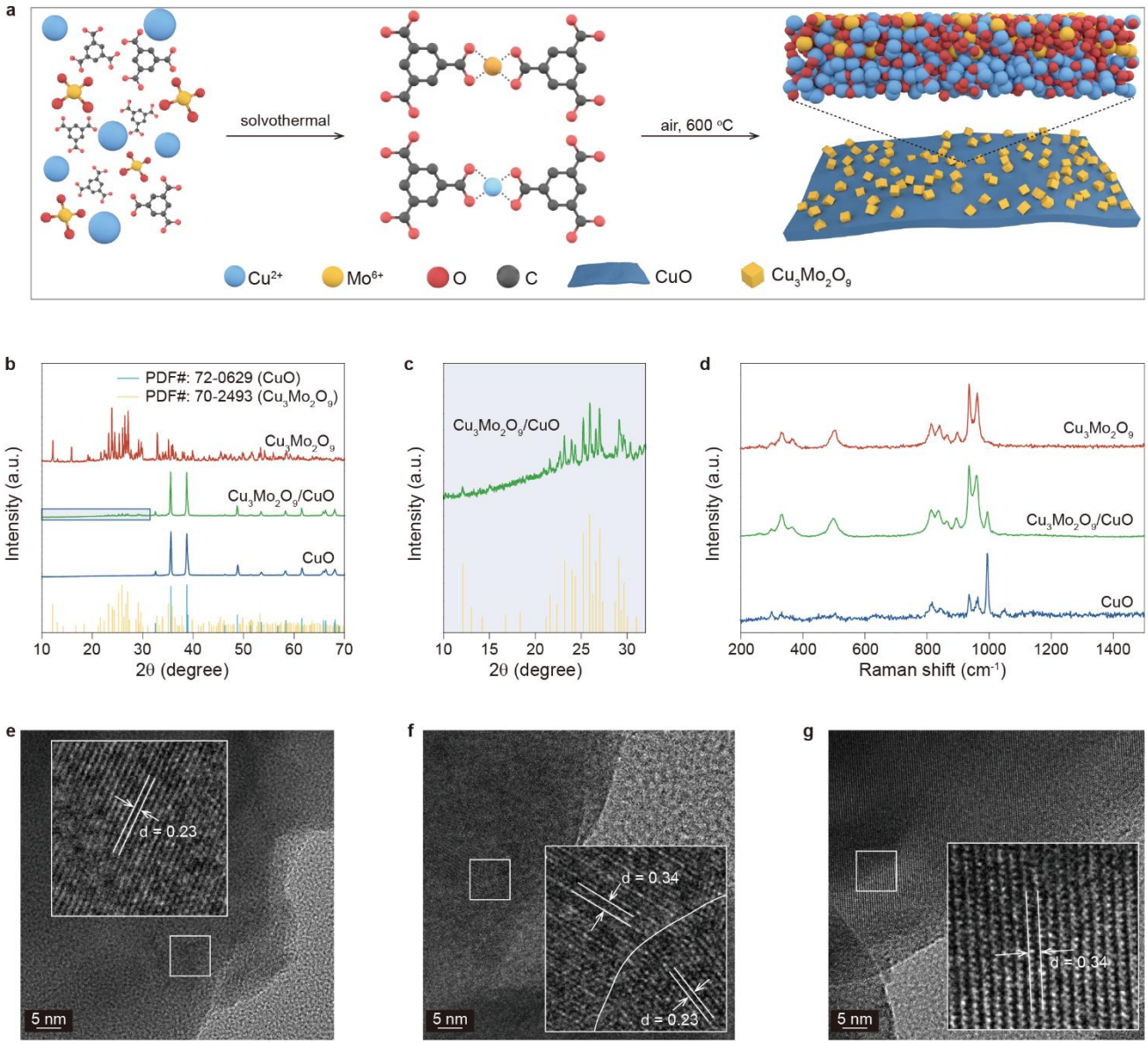

Figure 1. (a) Schematic illustration of the synthesis process for $Cu_3Mo_2O_9$/CuO. (b) XRD patterns of $Cu_3Mo_2O_9$/CuO, $Cu_3Mo_2O_9$, and CuO. (c) Magnified view of the green-boxed region in (b). (d) Raman spectra of $Cu_3Mo_2O_9$/CuO, $Cu_3Mo_2O_9$, and CuO. High-resolution TEM images of (e) CuO, (f) $Cu_3Mo_2O_9$/CuO, and (g) $Cu_3Mo_2O_9$.

$Cu_3Mo_2O_9$/CuO was synthesized by co-precipitation of a mixture of molybdenum chloride, copper chloride, in the presence of trimesic acid, followed by a calcination step under air (**Fig. 1a**). The crystal structures of the as-prepared catalysts were analyzed by X-ray diffraction (XRD). As shown in **Fig.**

1b-c, $Cu_3Mo_2O_9$/CuO exhibits a mixed-phase, comprising of orthorhombic $Cu_3Mo_2O_9$ (JCPDS No. 70-2493) and monoclinic CuO (JCPDS No. 72-0629).[27,28] Raman spectra (**Fig. 1d**) further confirm the coexistence of $Cu_3Mo_2O_9$ and CuO in $Cu_3Mo_2O_9$/CuO.[29] Scanning electron microscopy (SEM) measurements (**Fig. S1**) reveal that all of the as-prepared samples exhibit irregular block-like morphologies. Specifically, the SEM image of $Cu_3Mo_2O_9$/CuO displays large CuO particles serving as the substrate, with small $Cu_3Mo_2O_9$ nanoparticles dispersed on the surface. To further examine the local structures, transmission electron microscopy (TEM) measurements were conducted. High-resolution TEM (HR-TEM) images show lattice fringes with interplanar spacings of 0.23 nm and 0.34 nm in CuO (**Fig. 1e**) and $Cu_3Mo_2O_9$ (**Fig. 1g**), corresponding to the (111) plane of monoclinic CuO and the (002) plane of orthorhombic $Cu_3Mo_2O_9$, respectively. As shown in **Fig. 1f**, $Cu_3Mo_2O_9$/CuO consists of two distinct regions: one with low crystallinity, attributed to $Cu_3Mo_2O_9$, and the other with high crystallinity corresponding to CuO. Energy-dispersive X-ray spectroscopy (EDX) elemental mapping (**Fig. S2**) confirms the uniform distribution of Cu, Mo, and O elements in $Cu_3Mo_2O_9$/CuO. Based on the above characterization results, it can be concluded that the as-synthesized $Cu_3Mo_2O_9$/CuO catalyst exhibits a heterojunction structure.

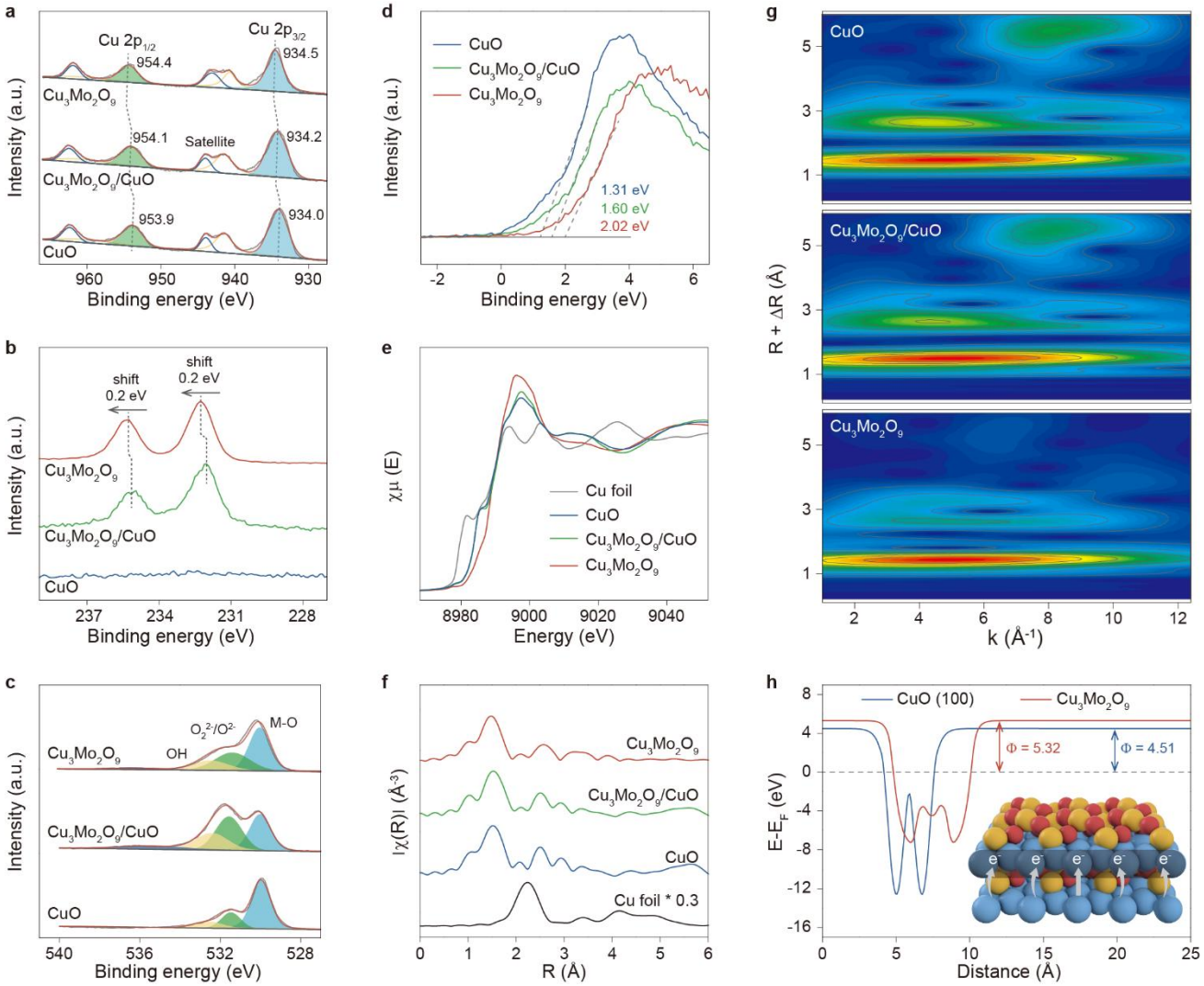

Figure 2. High-resolution XPS spectra of (a) Cu 2p, (b) Mo 3d, and (c) O 1s for $Cu_3Mo_2O_9$/CuO, CuO, and $Cu_3Mo_2O_9$. (d) Valence-band edge (VBE) spectra of $Cu_3Mo_2O_9$/CuO, CuO, and $Cu_3Mo_2O_9$. (e) Normalized XANES spectra at the Cu K-edge. (f) Fourier-transformed EXAFS (FT-EXAFS) spectra at the Cu K-edge in R-space for Cu foil, $Cu_3Mo_2O_9$/CuO, CuO, and $Cu_3Mo_2O_9$. (g) Wavelet transform (WT)-EXAFS contour plots of the Cu K-edge for CuO, $Cu_3Mo_2O_9$/CuO, and $Cu_3Mo_2O_9$. (h) Average Coulomb potential (eV) along the Z-axis (slab direction) in CuO (100) and $Cu_3Mo_2O_9$-terminated supercells. Inset illustrates the interfacial electron transfer in $Cu_3Mo_2O_9$/CuO.

X-ray photoelectron spectroscopy (XPS) measurements were performed to investigate the chemical states and bonding environments of the as-prepared samples. The Cu 2p XPS spectrum of $Cu_3Mo_2O_9$/CuO (**Fig. 2a**) exhibits characteristic peaks at 934.2 eV and 954.1 eV, corresponding to Cu^{2+} in the Cu $2p_{3/2}$ and Cu $2p_{1/2}$ region, respectively.[30,31] Compared to $Cu_3Mo_2O_9$/CuO, the Cu in $Cu_3Mo_2O_9$ displays a higher oxidation state, whereas that in CuO shows in a lower oxidation state. As

presented in **Fig. 2b**, the high-resolution Mo $3d_{5/2}$ XPS spectrum displays a peak at 232.1 eV, while the Mo $3d_{3/2}$ peak appears at 235.2 eV, indicating presence of Mo^{6+} in $Cu_3Mo_2O_9$/CuO.[32,33] Notably, the binding energy of Mo^{6+} species in $Cu_3Mo_2O_9$/CuO is negatively shifted by approximately 0.2 eV compared to that in $Cu_3Mo_2O_9$. The O 1s XPS spectra can be fitted into three peaks located at ~529.9 eV (metal–oxygen bonds, Cu-O/Mo-O), ~531.4 eV (lattice oxygen), and ~532.4 eV (surface hydroxyl/adsorbed oxygen) (**Fig. 2c**). These results are consistent with the coexistence of $Cu_3Mo_2O_3$ and CuO phases in the heterostructure.[34] The valence-band edge (V_{BE}) spectra (**Fig. 2d**) reveal distinct electronic structures among CuO, $Cu_3Mo_2O_9$, and $Cu_3Mo_2O_9$/CuO samples. The V_{BE} position of $Cu_3Mo_2O_9$/CuO (1.60 eV) is located in-between that of CuO (1.31 eV) and $Cu_3Mo_2O_9$ (2.02 eV), implying electronic interactions between $Cu_3Mo_2O_9$ and CuO.[35] To further investigate the valence states and local coordination environments, X-ray absorption spectroscopy (XAS) measurements were performed. X-ray absorption near-edge structure (XANES) spectra at the Cu K-edge (**Fig. 2e and Fig. S3a**) reveal an increase of Cu valence state in $Cu_3Mo_2O_9$/CuO as compared to that in CuO. The Fourier-transformed extended X-ray absorption fine structure (FT-EXAFS) spectra (**Fig. 2f**) exhibit a prominent peak at 1.5 Å, matching well with the Cu-O characteristic peak in CuO.[36,37] The wavelet transform (WT) contour plot of the Cu K-edge for the reference Cu foil (**Fig. S3b**) displays an intensity maximum at 7.2 $Å^{-1}$, attributable to Cu-Cu interactions. In contrast, that for the CuO, $Cu_3Mo_2O_9$, and $Cu_3Mo_2O_9$/CuO samples exhibit a single intensity maximum at around 4.6 $Å^{-1}$, corresponding to Cu-O (**Fig. 2g**).[38] The above characterization results from TEM, XPS, and XAS together with DFT calculations (**Fig. 2h**) confirm the successful formation of $Cu_3Mo_2O_9$/CuO heterostructured, with strong electronic interactions.

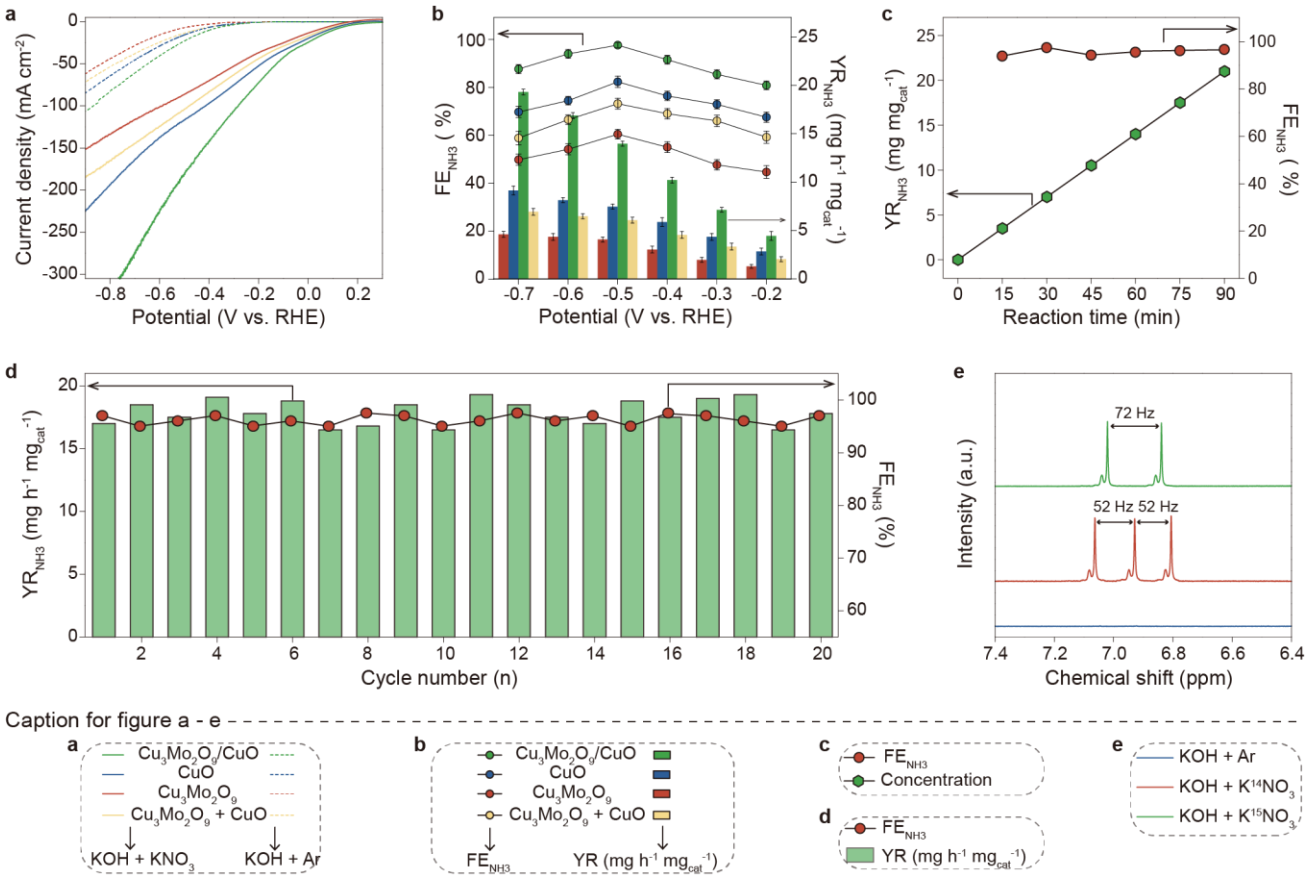

Figure 3. (a) Linear sweep voltammetry (LSV) curves recorded in 1 M KOH solution with or without 0.05 M KNO_3. (b) NH_3 Faradaic efficiency (FE) and NH_3 yield rate over $Cu_3Mo_2O_9$/CuO, CuO, $Cu_3Mo_2O_9$, and a physical mixture of $Cu_3Mo_2O_9$ + CuO at different applied potentials (the reported potentials are not iR-corrected). (c) Time-dependent NH_3 concentration and FE over $Cu_3Mo_2O_9$/CuO at -0.5 V vs. RHE. (d) Cyclic stability test of $Cu_3Mo_2O_9$/CuO. (e) ^1H nuclear magnetic resonance (NMR) spectra for NH_4^+ quantification.

The electrochemical NO_3^-RR performance was evaluated in a standard H-type electrolysis cell. As shown in **Fig. 3a**, the linear sweep voltammetry (LSV) curves show that all of the examined catalysts exhibit a significantly higher current density in KNO_3/KOH solution compared to pure KOH solution, indicating enhanced activity toward NO_3^-RR. $Cu_3Mo_2O_9$/CuO shows the highest current density, reaching 300 mA cm^{-2} at -0.75 V vs. RHE. The NO_3^-RR products were quantified by the indophenol blue method and Ion chromatography method (**Fig. S4**). As the applied cathodic potential increased from -0.2 to -0.7 V vs. RHE, the NH_3 Faradaic efficiency (FE_{NH_3}) first increased and then decreased, while the NH_3 yield rate (YR_{NH_3}) progressively increased (**Fig. 3b**). At higher cathodic potentials, a slight decline in FE_{NH_3} was observed due to the competing HER. Remarkably, $Cu_3Mo_2O_9$/CuO achieved a maximum FE_{NH_3} of 97.5% at -0.5 V vs. RHE, corresponding to an NH_3 partial current density of 176.5 mA cm^{-2} (**Fig. S5**). Additionally, a highest YR_{NH_3} of 19.3 mg h^{-1} mg_{cat}^{-1} was recorded

at -0.7 V vs. RHE. In contrast, the electrocatalytic activity of a physical mixture of $Cu_3Mo_2O_9$ + CuO was significantly lower than that of $Cu_3Mo_2O_9$/CuO, suggesting that the interfacial interaction between $Cu_3Mo_2O_9$ and CuO was beneficial for enhancing the NO_3^-RR. Besides NH_3, nitrite (NO_2^-) was also detected as a NO_3^-RR byproduct, and its Faradaic efficiency decreased as the applied potential became more negative (**Fig. S6**). Furthermore, the NH_3 yield over $Cu_3Mo_2O_9$/CuO increased steadily with electrolysis time, while the FE_{NH_3} remained stable at ~97% for up to 90 minutes (**Fig. 3c**). As shown in **Fig. 3d**, after 20 consecutive electrolysis cycles, both FE_{NH_3} and YR_{NH_3} exhibited little fluctuations, demonstrating the remarkable reusability and stability of $Cu_3Mo_2O_9$/CuO. The differences in Faradaic electron transfer processes and diffusion processes were investigated by electrochemical impedance spectroscopy (EIS) on $Cu_3Mo_2O_9$/CuO and CuO (**Fig. S8**). The Nyquist plots clearly reveal that $Cu_3Mo_2O_9$/CuO exhibits a smaller semicircle than CuO, corresponding to a lower charge-transfer resistance. This result demonstrates that the heterostructure can facilitate faster electron transfer, which is consistent with the improved NO_3^-RR activity. The EIS results therefore provide confirmation of the superior reaction kinetics of the $Cu_3Mo_2O_9$/CuO catalyst. To verify the nitrogen source of the produced NH_3, isotopically labeled $^{15}NO_3^-$ was used as the reactant. The ^{1}H nuclear magnetic resonance (NMR) spectra (**Fig. 3e** and **S9**) exhibited characteristic double peaks with a separation of 72 Hz, corresponding to $^{15}NH_4^+$, confirming that NH_3 was indeed derived from NO_3^-RR rather than environmental contamination.

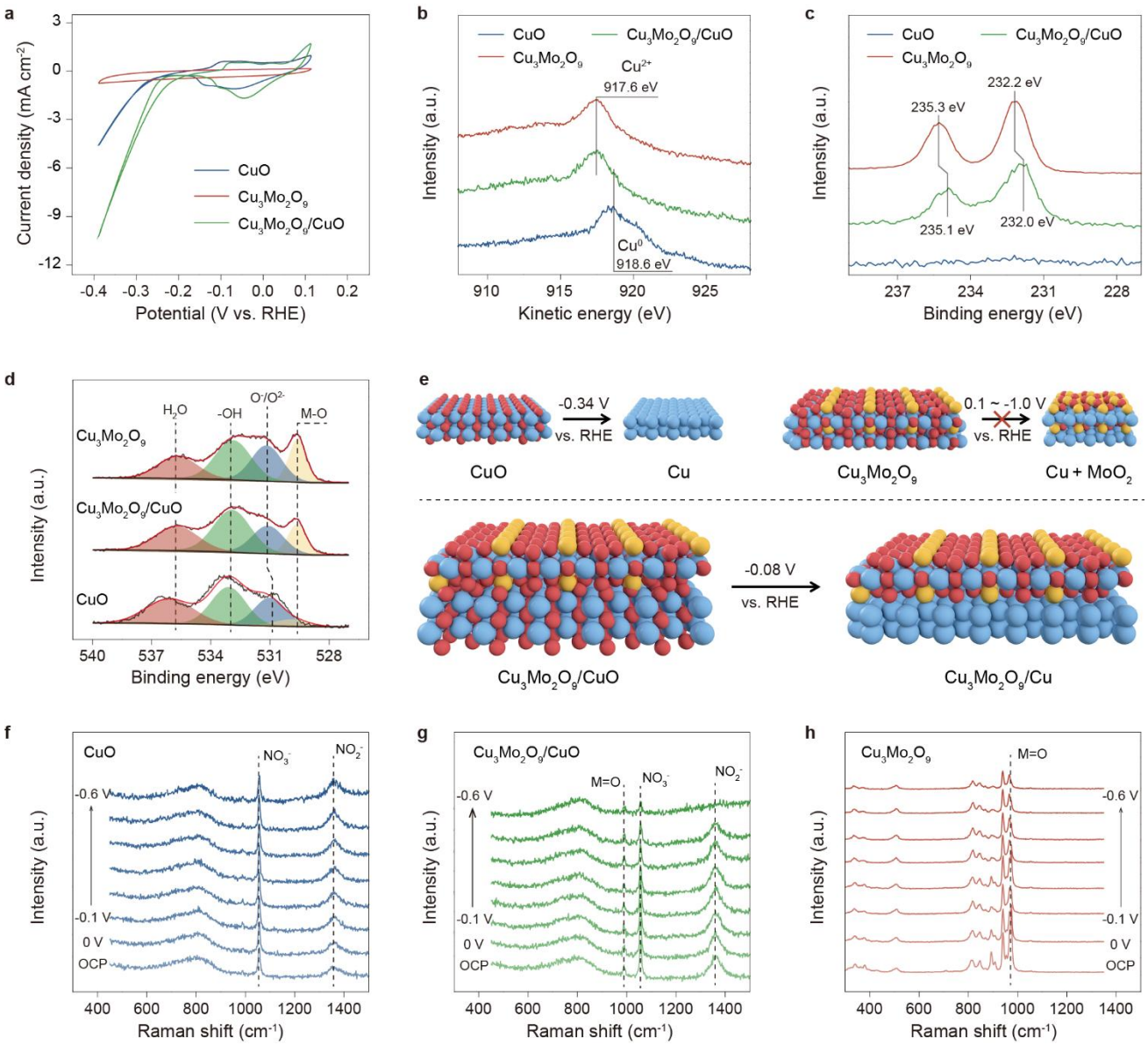

Figure 4. (a) CV curves of $Cu_3Mo_2O_9$/CuO, CuO and $Cu_3Mo_2O_9$ recorded in 1 M KOH solution. (b) The Cu auger electron spectroscopy spectra of post-reaction $Cu_3Mo_2O_9$/CuO, CuO and $Cu_3Mo_2O_9$. (c) High-resolution Mo XPS spectra of post-reaction $Cu_3Mo_2O_9$/CuO and $Cu_3Mo_2O_9$. (d) High-resolution O XPS spectra of post-reaction $Cu_3Mo_2O_9$/CuO, CuO and $Cu_3Mo_2O_9$. (e) The phase evolution diagram of $Cu_3Mo_2O_9$/CuO, CuO and $Cu_3Mo_2O_9$ during the NO_3^-RR. *In-situ* Raman spectra recorded over (f) CuO, (g) $Cu_3Mo_2O_9$/CuO and (h) $Cu_3Mo_2O_9$.

Subsequently, the electrochemical stability and phase evolution of the as-prepared catalysts were systematically investigated using multiple *in-situ* characterization techniques. Cyclic voltammetry (CV) analysis (**Fig. 4a**) reveals that $Cu_3Mo_2O_9$ exhibits no distinct reduction peak during cathodic scan, in sharp contrast to CuO-containing catalysts, which display pronounced reduction features at -0.05 to

-0.2 V vs. RHE. This suggests that $Cu_3Mo_2O_9$ possesses superior redox stability as compared to the easily reducible CuO. To further confirm that this process occurs in the composite system, a comparative CV test was conducted on the physically mixed $Cu_3Mo_2O_9$ + CuO (**Fig. S10**). The mixed sample displays distinct, separate reduction features corresponding to CuO and $Cu_3Mo_2O_9$, whereas the $Cu_3Mo_2O_9$/CuO heterostructure exhibits broadened and shifted peaks, consistent with interfacial electronic interactions facilitating CuO-to-Cu reduction rather than independent phase behavior. Powder XRD after electrolysis reveals the emergence of diffraction peaks assignable to metallic Cu [(111), (200), (220)] alongside the preserved $Cu_3Mo_2O_9$ reflections (**Fig. S11**). This indicates that Cu^0 not only forms but also crystallizes with sufficient domain size to be detected by XRD, proving that it is structurally stable and not merely a trace surface artifact. To further elucidate the electrochemical stability, *ex-situ* Cu Auger electron spectroscopy (AES) measurements were conducted. The results (**Fig. 4b**) show a negligible chemical shift (Δ = + 0.1 eV) for $Cu_3Mo_2O_9$ after NO_3^-RR, whereas CuO-containing catalysts after NO_3^-RR exhibit significant negative shifts (Δ = 0.8-1.2 eV), indicative of $Cu^{2+} \rightarrow Cu^0$ reduction.[39] This observation was corroborated by the post-reaction Cu 2p XPS spectra (**Fig. S12**). Complementary Mo 3d (**Fig. 4c**) and O 1s (**Fig. 4d**) XPS analyses further confirm the structural integrity of $Cu_3Mo_2O_9$.[32] Indeed, the Mo^{6+} oxidation state remained unchanged, and the metal-oxygen (Mo-O) bonds were preserved throughout the NO_3^-RR. In contrast, the disappearance of Cu-O signal in the CuO-containing catalysts (**Fig. 4d**) indicates the complete reduction of CuO to metallic Cu.[40] These signatures unambiguously confirm the generation of Cu^0 domains. In addition, quantitative fitting shows an increasing Cu^0/Cu^{2+} ratio as the potential becomes more negative (**Fig. S13**), verifying that the metallic state is stabilized under NO_3^-RR conditions. The samples collected after extended NO_3^-RR electrolysis were examined by STEM-EELS mapping to directly validate the interfacial structure. The elemental distribution maps show co-localization of Cu (L-edge) and Mo-O (M-edge, O-K edge) signals at contiguous nanoscale domains, with line-profiles across particle boundaries confirming intimate contact between metallic Cu and $Cu_3Mo_2O_9$ regions (**Fig. S14c-d**). These results provide direct visualization of the heterointerface, supporting our earlier spectroscopic assignments. Complementary STEM-EDX elemental mapping shows a similar pattern: Cu signals are enriched at reduced domains, while Mo and O remain associated with the oxide framework, demonstrating that Cu domains form *in-situ* and are spatially anchored to the $Cu_3Mo_2O_9$ matrix rather than dispersed randomly (**Fig. S14a-b**). The dynamic catalyst structure evolution during NO_3^-RR is

schematically summarized in **Fig. 4e**. Under mild reductive conditions, CuO readily transforms into metallic Cu, whereas $Cu_3Mo_2O_9$ can maintain its structural integrity. Previous studies have demonstrated that the reduction of $Cu_3Mo_2O_9$ to metallic Cu and MoO_2 requires a hydrogen (H_2) atmosphere at elevated temperatures.[41] This thermodynamic stability explains the operational durability of the $Cu_3Mo_2O_9$/CuO catalyst under nitrate reduction conditions (typically < -0.6 V vs. RHE), in which, selective reduction of CuO to metallic Cu occurs while $Cu_3Mo_2O_9$ remains intact, leading to the *in-situ* formation of an active $Cu_3Mo_2O_9$/Cu catalytic phase. The stability of $Cu_3Mo_2O_9$ during NO_3^-RR was further confirmed by *in-situ* Raman spectroscopy (**Fig. 4f-h**). Characteristic peaks of $Cu_3Mo_2O_9$ in the wavenumber region of 800-1000 cm^{-1} are well maintained in the applied cathodic potential range from 0 to -0.6 V vs. RHE, demonstrating its resistance to electrochemical reduction.[42] The selective reduction of CuO to metallic Cu, coupled with the preservation of $Cu_3Mo_2O_9$ during NO_3^-RR, enables the formation of an active and stable catalytic surface, enhancing both the NO_3^-RR activity and durability.

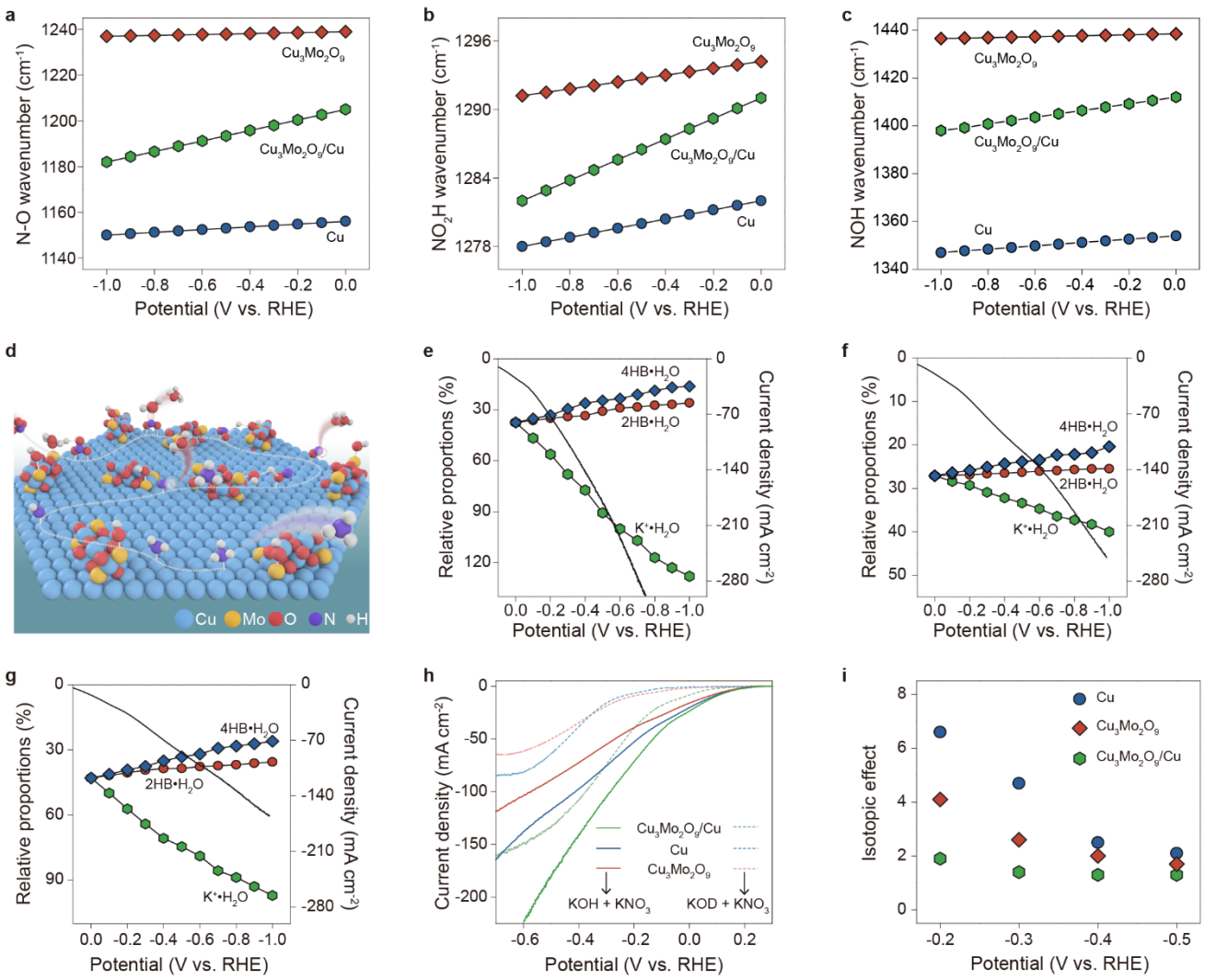

Figure 5. Potential-dependent infrared absorption spectroscopy wavenumber for (a) NO, (b) NO_2H and (c) NOH. (d) Schematic illustration showing electrocatalytic nitrate-to-ammonia reaction pathway on $Cu_3Mo_2O_9$/Cu. Potential-dependent relative proportion of interfacial water over (e) $Cu_3Mo_2O_9$/Cu, (f) Cu and (g) $Cu_3Mo_2O_9$ and the corresponding NO_3^-RR current density. The relative proportion was obtained by dividing the proportion of each component by its corresponding peak area at 0 V vs. RHE to eliminate the experimental error. (h) Linear sweep voltammetry curves recorded in 1 M KOH/H_2O solution with 0.05 M KNO_3 and 1 M KOD/D_2O solution with 0.05 M KNO_3. (i) The isotope effect of $Cu_3Mo_2O_9$/Cu, Cu and $Cu_3Mo_2O_9$.

To unravel the reaction pathway and intermediate species involved in the NO_3^-RR over $Cu_3Mo_2O_9$/Cu, $Cu_3Mo_2O_9$ and Cu, *in-situ* attenuated total reflectance surface-enhanced infrared spectroscopy (ATR-SEIRAS)[43,44] measurements were performed (**Fig. S15**). Distinct vibrational signals emerged in the spectral profiles of the three catalysts with increasing cathodic potential (**Fig.**

S16-S18). Peaks at ~1205 cm^{-1} and 2107 cm^{-1} are assigned to *N-O stretching modes, while bands at 1292 cm^{-1} and 1409 cm^{-1} arise from *NO-H_x vibrations; together these features evidence the progressive deoxygenation of nitrate on the surface.[45,46] Notably, making the potential more cathodic induces small, reproducible blue shifts (typically + 3-20 cm^{-1}) in the *NO, *NO_2H, and *NOH vibrations and increases their intensities, consistent with Stark-tuning and higher surface coverage under cathodic bias (**Fig. 5a-c**).[47] Comparative analysis revealed analogous adsorption dynamics for *NO, *NO_2H, and *NOH on $Cu_3Mo_2O_9$/Cu and Cu, suggesting shared intermediate binding characteristics. Further spectral deconvolution identified broad bands at 1625 cm^{-1} (H_2O bending) and 1668 cm^{-1} (N-H σ bending), signifying hydrogenation-driven NH_3 formation post-deoxygenation. Based on the above *in-situ* characterizations, a reaction pathway is proposed as shown in **Fig. 5d** where the adsorbed *NO_3^- species undergoes sequential oxygen removal to *NO_2^- and *NO, followed by proton-coupled hydrogenation to NH_3, with interfacial H_2O serving as the primary proton donor in alkaline media.[48,49] To probe the influence of interfacial H_2O on electrochemical NO_3^-RR over the three catalysts, the O-H stretching regions (2500-3800 cm^{-1}) in the ATR-SEIRAS spectra was analyzed. Gaussian fit of three O-H stretching modes revealing three distinct components (the half-width at half-maximum remains consistent for same component): 4-coordinated hydrogen-bonded water (4-HB•H_2O, low wavenumber component, blue), 2-coordinated hydrogen-bonded water (2-HB•H_2O, primary component, red) and K^+ ion hydrated water (K•H_2O, high wavenumber component, green) (**Fig. 5e-g** and **Fig. S19**).[50,51] The presence of K•H_2O on the catalyst's surface is attributed to the migration of K^+ cations for charge compensation at negative potentials.[52] To maintain the data rationality, the full width at half maximum (FWHM) of each component at different bias voltages was kept the same. While 4-HB•H_2O and 2-HB•H_2O proportions remained relatively stable over the three catalysts, K•H_2O accumulation intensified markedly on $Cu_3Mo_2O_9$/Cu, which might explain the higher NO_3^-RR activity over $Cu_3Mo_2O_9$/Cu than $Cu_3Mo_2O_9$ and Cu. The isotopic effect[53] further validated the superior water dissociation capability on the $Cu_3Mo_2O_9$/Cu catalyst: in comparative experiments where H_2O was replaced by D_2O, $Cu_3Mo_2O_9$/Cu exhibited the least current density decay (**Fig. 5h-i**).

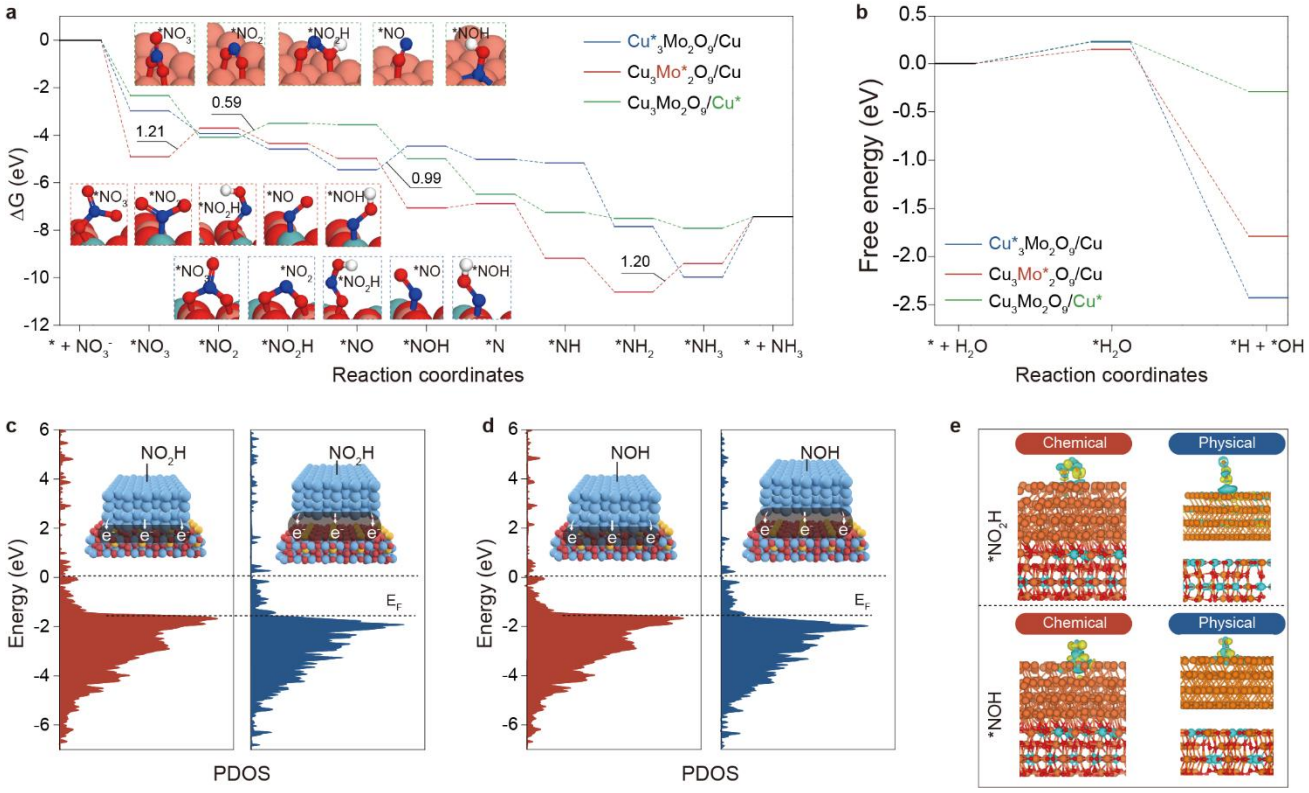

Figure 6. (a) Reaction free energies of NO_3^-RR on $Cu^*_3Mo_2O_9$/Cu, $Cu_3Mo^*_2O_9$/Cu and $Cu_3Mo_2O_9/Cu^*$ (the NO_3^- adsorption sites are highlighted using color coding and asterisk "*" label, and Cu* metal is based on Cu*(111) model). (b) H_2O dissociation free energies on $Cu^*_3Mo_2O_9$/Cu, $Cu_3Mo^*_2O_9$/Cu and $Cu_3Mo_2O_9/Cu^*$ (the H_2O adsorption sites are highlighted using color coding and asterisk "*" label). Projected density of states (PDOS) for (c) *NO_2H and (d) *NOH on $Cu_3Mo_2O_9$/Cu and physically mixed $Cu_3Mo_2O_9$ and Cu ($Cu_3Mo_2O_9$+Cu). The inset shows the *NO_2H and * NOH adsorption. (e) Charge density distribution of $Cu_3Mo_2O_9$/Cu and physically mixed $Cu_3Mo_2O_9$ and Cu ($Cu_3Mo_2O_9$ + Cu) during adsorption of intermediates (*NO_2H and *NOH). The faint yellow and cyan regions refer to the increased and decreased charge densities, respectively.

To provide a deep theoretical understanding of the NO_3^-RR on $Cu_3Mo_2O_9$/Cu, density functional theory (DFT) calculations were performed. Three models including $Cu_3Mo_2O_9$/Cu, $Cu_3Mo_2O_9$ and Cu were constructed to represent the $Cu_3Mo_2O_9$/CuO, $Cu_3Mo_2O_9$ and CuO catalysts. It should be noted that the DFT simulations were performed using a static slab model under implicit solvation and fixed-charge boundary conditions. These calculations capture qualitative interfacial trends rather than reproduce explicit dynamic, electrolyte, or constant-potential effects. Hence, the mechanistic insights should be interpreted as representative trends consistent with experimental observations rather than quantitative potential-dependent dynamics. The free energies of NO_3^-RR were calculated, and the

results are shown in **Fig. 6a**. The conversion of *NO_3 to *NO_2 on the Mo site of $Cu_3Mo_2O_9$/Cu requires overcoming an energy barrier of 1.21 eV. Over $Cu^*_3Mo_2O_9$/Cu site, the formation of *NOH from *NO (0.99 eV) was the potential-determining step (PDS). The PDS changed to the formation of *NO_2H with a greatly reduced Gibbs free energy barrier of 0.59 eV on $Cu_3Mo_2O_9/Cu^*$, indicating a higher NO_3^-RR activity. Additionally, the PDS for pure $Cu_3Mo_2O_9$ and Cu (**Fig. S20a**) are the formation steps of *NH_3 (1.69 eV) and *NOH (1.14 eV), respectively. The influence of Cu crystal planes and layer number on the reaction free energy of $Cu_3Mo_2O_9$/Cu was also investigated via DFT calculations. The results (**Fig. S21-25**) indicate that the Cu(111) plane was more conducive to reducing the energy barrier, while the layer number has little effect on the energy and adsorption state. Projected crystal orbital Hamilton population (pCOHP) analysis was further performed to understand the NO_3^- activation process (**Fig. S26**). By integrating the energy up to the Fermi level, the integrated COHP (ICOHP) was calculated. The ICOHP value changes from -15.47 (NO_3^- adsorbed on $Cu_3Mo^*_2O_9$/Cu) to -15.05 (NO_3^- adsorbed on $Cu_3Mo_2O_9/Cu^*$), giving a clear hint for the more effective NO_3^- adsorption and activation on Cu sites.[54-56] Furthermore, $Cu_3Mo^*_2O_9$/Cu exhibits a much better water dissociation capability as compared to $Cu_3Mo_2O_9/Cu^*$, $Cu^*_3Mo_2O_9$/Cu, $Cu_3Mo_2O_9$ and Cu (**Fig. 6b** and **Fig. S20b**), which shall greatly benefit the hydrogenation process. To further investigate the crucial role played by the $Cu_3Mo_2O_9$–Cu interface in $Cu_3Mo_2O_9$/Cu toward boosting NO_3^-RR kinetics, we calculated the total density of states (DOS) and projected density of states (PDOS) for both $Cu_3Mo_2O_9$/Cu and physically mixed $Cu_3Mo_2O_9$ + Cu **(Fig. 6c** and **6d**). The results indicate that under *NO_2H and *NOH adsorption conditions, the d-band center of $Cu_3Mo_2O_9$/Cu shifts upward toward the Fermi level, which modulates the adsorption energies of *NO_2H and *NOH to facilitate the subsequent deoxygenation processes. Concurrently, charge density difference analysis (**Fig. 6e**) demonstrates stronger electron cloud localization around $Cu_3Mo_2O_9$/Cu as compared to physically mixed $Cu_3Mo_2O_9$ + Cu during *NO_2H and *NOH adsorption, suggesting enhanced interfacial interactions between $Cu_3Mo_2O_9$/Cu and the adsorbed *NO_2H/*NOH species.

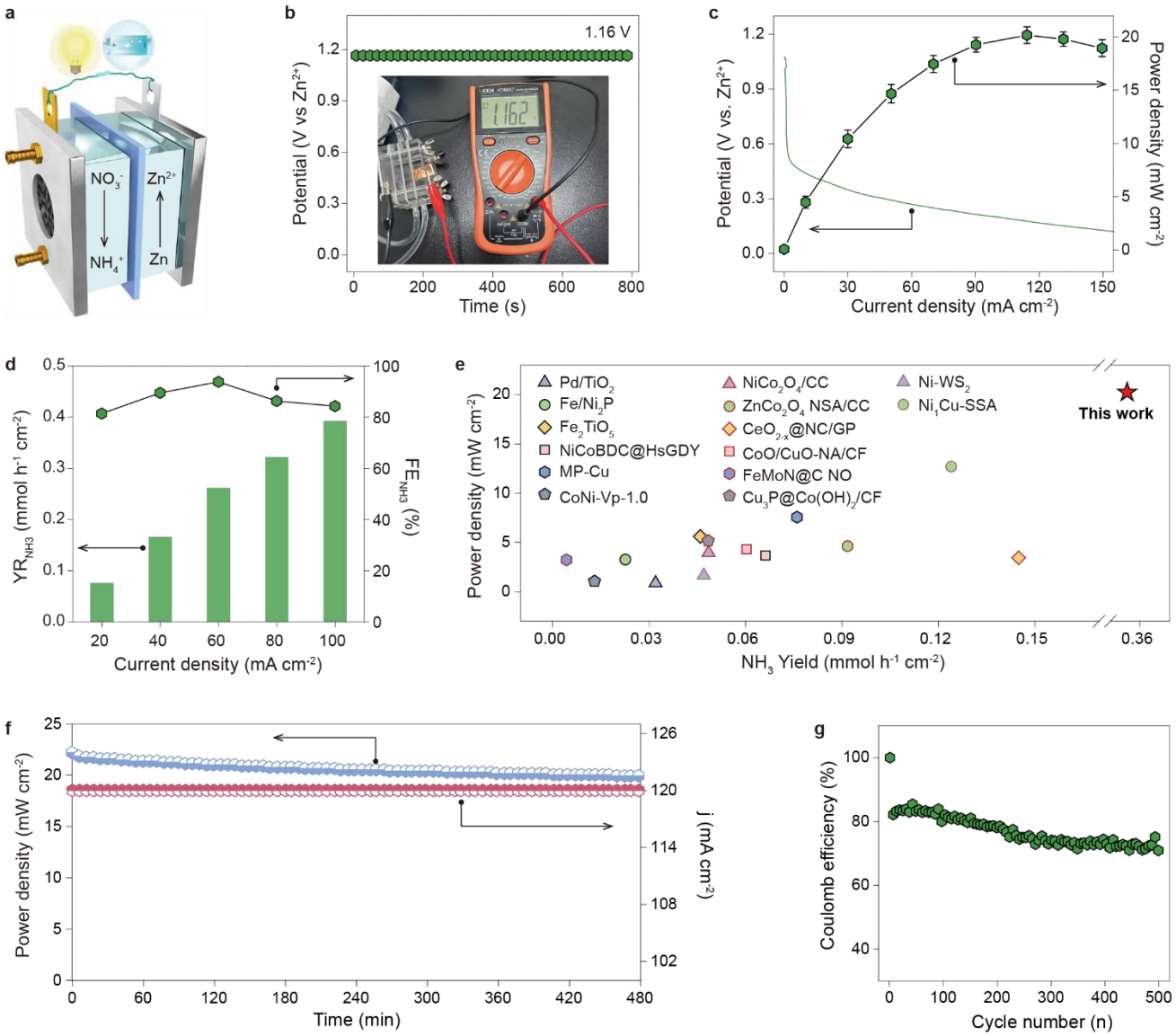

Figure 7. (a) Schematic representation of a Zn-nitrate battery. (b) Open circuit voltage of the Zn-nitrate battery with $Cu_3Mo_2O_9$/Cu cathode. (c) The discharging polarization curve and the resultant power density of the Zn-nitrate battery with $Cu_3Mo_2O_9$/Cu cathode (the reported potentials are not iR-corrected). (d) FE_{NH3} and NH_3 yield rate of the Zn-nitrate battery with $Cu_3Mo_2O_9$/Cu cathode. (e) Comparison of the Zn-nitrate battery performance.[5,57-69] (f) Stability tests of the Zn-NO_3^- battery at 120 mA cm^{-2}. (g) The coulombic efficiency of the Zn-NO_3^- battery for 500 cycles.

To demonstrate the application potential, the as-prepared $Cu_3Mo_2O_9$/Cu was applied as the cathode catalyst to assemble Zn-nitrate batteries (**Fig. 7a**). As shown in **Fig. 7b**, the Zn-nitrate battery with the $Cu_3Mo_2O_9$/Cu cathode displays an open-circuit voltage (OCV) of ~1.16 V vs Zn^{2+}, which is capable to deliver a maximum power density of 20.24 mW cm^{-2} at 0.17 V vs Zn^{2+} (**Fig. 7c**), achieving the highest NH_3 yield and FE_{NH_3} of 0.393 mmol h^{-1} cm^{-2} and 93.8% at 100 mA cm^{-2} and 60 mA cm^{-2},

respectively (**Fig. 7d**), surpassing most of the reported values in the literature (**Fig. 7e**). Then, a long-term discharge test of the Zn-nitrate battery assembled by the $Cu_3Mo_2O_9$/Cu cathode was conducted at the 120 mA cm^{-2} corresponding to the maximum power density, as shown in **Fig. 7f**, with a steady Coulombic efficiency over 500 cycles (**Fig. 7g**), demonstrating the excellent reusability and stability of $Cu_3Mo_2O_9$/Cu.

Conclusions

In summary, we have developed a heterostructured $Cu_3Mo_2O_9$/CuO catalyst that can be *in-situ* reconstructed into active $Cu_3Mo_2O_9$/Cu during electrochemical NO_3^-RR. This architecture leverages spatially decoupled active sites: the $Cu_3Mo_2O_9$ is proposed to facilitate H_2O dissociation and likely contribute to protons (H^+) supply, while the metallic Cu facilitates NO_3^- adsorption and the subsequent deoxygenation. Consequently, the active $Cu_3Mo_2O_9$/Cu catalyst achieves an exceptional NH_3 Faradaic efficiency of 97.5% at -0.5 V vs. RHE with an excellent NH_3 yield rate of 19.3 mg h^{-1} mg_{cat}^{-1} in electrochemical NO_3^-RR. When applied as the cathode catalyst, the assembled Zn-nitrate battery delivers a peak power density of 20.24 mW cm^{-2} with an FE_{NH3} of 93.8% at 60 mA cm^{-2}. Our work shall pave the way for engineering efficient catalysts for complex reactions such as CO_2 reduction and nitrogen fixation, where dynamic interfacial interactions are critical to achieving high activity and selectivity.

Author Contributions

H. Qi, C. Su, and B. Liu conceived and designed the experiments. J. Ni, J. Yan, S. Huang and W. Wang carried out synthesis of catalysts and performed experiments on performance testing. L. Liu, J. Ding, and H. Sun contributed to the data analysis. Y. Tao performed the DFT calculation. A. Chachvalvutikul and O. Akdim contributed to the revision of the manuscript. H. Qi, and B. Liu supervised the entire project.

Acknowledgments

This work was supported by the National Key Research and Development Program of China (2021YFA1600800), National Natural Science Foundation of China (22372102, 22102102, 21902105), Educational Commission of Guangdong Province (2021ZDZX2036), Shenzhen Science and Technology Program (RCJC20200714114434086, 20231122120657001), Research Team Cultivation Program of Shenzhen University (2023QNT013), State-sponsored Postdoctoral Researcher program

(Grant NO. GZC20231716), the City University of Hong Kong startup fund (9020003), ITF-RTH-Global STEM Professorship (9446006), JC STEM lab of Advanced CO_2 Upcycling (9228005), the arie Skłodowska-Curie Actions Postdoctoral Fellowships (101107009-AtomCat4Fuel) and UKRI (EP/Y029305/1).

References

1. K. Liu, Z. Sun, X. Peng, X. Liu, X. Zhang, B. Zhou, K. Yu, Z. Chen, Q. Zhou, F. Zhang, Y. Wang, X. Gao, W. Chen and P. Chen, *Nat. Commun.*, 2025, **16**, 2167.
2. T. Huang, T. Liang, J. You, Q. Huo, S. Qi, J. Zhao, N. Meng, J. Liao, C. Shang, H. Yang, Q. Hu and C. He, *Energy Environ. Sci.*, 2024, **17**, 8360.
3. L. Liu, T. Xiao, H. Fu, Z. Chen, X. Qu and S. Zheng, *Appl. Catal. B: Environ.*, 2023, **323**, 122181.
4. H. Jiang, G.-F. Chen, O. Savateev, J. Xue, L.-X. Ding, Z. Liang, M. Antonietti and H. Wang, *Angew. Chem., Int. Ed.*, 2023, **62**, e202218717.
5. Y. Guo, R. Zhang, S. Zhang, Y. Zhao, Q. Yang, Z. Huang, B. Dong and C. Zhi, *Energy Environ. Sci.*, 2021, **14**, 3938.
6. W. Yu, J. Yu, M. Huang, Y. Wang, Y. Wang, J. Li, H. Liu and W. Zhou, *Energy Environ. Sci.*, 2023, **16**, 2991.
7. R. Jia, Y. Wang, C. Wang, Y. Ling, Y. Yu, and B. Zhang, *ACS Catal.*, 2020, **10**, 3533-3540.
8. Z.-Y. Wu, M. Karamad, X. Yong, Q. Huang, D. A. Cullen, P. Zhu, C. Xia, Q. Xiao, M. Shakouri, F.-Y. Chen, J. Y. Kim, Y. Xia, K. Heck, Y. Hu, M. S. Wong, Q. Li, I. Gates, S. Siahrostami and H. Wang, *Nat. Commun.*, 2021, **12**, 2870.
9. Z. Gong, X. Xiang, W. Zhong, C. Jia, P. Chen, N. Zhang, S. Zhao, W. Liu, Y. Chen and Z. Lin, *Angew. Chem. Int., Ed.*, 2023, **135**, e202308775.
10. G.-F. Chen, Y. Yuan, H. Jiang, S. Y. Ren, L. X. Ding, L. Ma, T. Wu, J. Lu and H. Wang, *Nat. Energy*, 2020, **5**, 605-613.
11. Y. Bu, C. Wang, W. Zhang, X. Yang, J. Ding and G. Gao, *Angew. Chem. Int. Ed.*, 2023**, 62***,* e202217337.
12. Y. Zhou, R. Duan, H. Li, M. Zhao, C. Ding and C. Li, *ACS Catal.*, 2023, **13**, 10846-10854.
13. L. Wu, J. Feng, L. Zhang, S. Jia, X. Song, Q. Zhu, X. Kang, X. Xing, X. Sun and B. Han, *Angew. Chem., Int. Ed.*, 2023, **62**, e202307952.
14. S. Zhang, J. Wu, M. Zheng, X. Jin, Z. Shen, Z. Li, Y. Wang, Q. Wang, X. Wang, H. Wei, J. Zhang, P. Wang, S. Zhang, L. Yu, L. Dong, Q. Zhu, H. Zhang and J. Lu, *Nat. Commun.*, 2023, **14**, 3634.
15. Z. Fang, Z. Jin, S. Tang, P. Li, P. Wu, and G. Yu, *ACS Nano*, 2022, **16**, 1072-1081.
16. J. Ni, J. Yan, F. Li, H. Qi, Q. Xu, C. Su, L. Sun, H. Sun, J. Ding and B. Liu, *Adv. Energy Mater.*, 2024, 2400065.
17. Y. Li, Z. Lu, L. Zheng, X. Yan, J. Xie, Z. Yu, S. Zhang, F. Jiang and H. Chen, *Energy Environ. Sci.*, 2024, **17**, 4582.
18. G. Zhang, X. Li, K. Chen, Y. Guo, D. Ma and K. Chu, *Angew. Chem., Int. Ed.*, 2023, **62**, e202300054.
19. Y. Wang, F. Hao, H. Xu, M. Sun, X. Wang, Y. Xiong, J. Zhou, F. Liu, Y. Hu, Y. Ma, X. Meng, L. Guo, C. Wang, M. Shao, G. Wang, J. Wang, P. Lu, J. Yin, J. Wang, W. Niu, C. Ye, Q. Zhang, S. Xi, B. Huang, M. Shao, Z. Fan, *Angew. Chem., Int. Ed.*, 2025, **64**, e202508617.
20. S. Zheng, X. Yang, Z.-Z. Shi, H. Ding, F. Pan, J.-F. Li, *J. Am. Chem. Soc.*, 2025, **146**, 26965-26974.

21. Y. Wan, M. Pei, Y. Tang, Y. Liu, W. Yan, J. Zhang, R. Lv, *Adv. Mater.*, 2025, **37**, 2417696.
22. Y. Liu, J. Ding, F. Li, X. Su, Q. Zhang, G. Guan, F. Hu, J. Zhang, Q. Wang, Y. Jiang, B. Liu and H. B. Yang, *Adv. Mater.*, 2023, **35**, 2207114.
23. Q. Wang, S.-F. Hung, K. Lao, X. Huang, F. Li, H. B. Tao, H. B. Yang, W. Liu, W. Wang, Y. Cheng, N. Hiraoka, L. Zhang, J. Zhang, Y. Liu, J. Chen, Y. Xu, C. Su, J. G. Chen and Bin Liu, *Nat. Catal.*, 2025, **8**, 378-388.
24. Y. Liu, Q. Wang, J. Zhang, J. Ding, Y. Cheng, T. Wang, J. Li, F. Hu, H. B. Yang and B. Liu, *Adv. Energy Mater.*, 2022, **12**, 2200928.
25. Q. Sha, S. Wang, L. Yan, Y. Feng, Z. Zhang, S. Li, X. Guo, T. Li, H. Li, Z. Zhuang, D. Zhou, B. Liu and X. Sun, *Nature*, 2025, **639**, 360-367.
26. J. Ding, H. Bin Yang, X.-L. Ma, S. Liu, W. Liu, Q. Mao, Y. Huang, J. Li, T. Zhang and B. Liu, *Nat. Energy*, 2023, **8**, 1386-1394.
27. N. F. Dummer, Z. Sodiq-Ajala, D. J. Morgan and T. E. Davies, *Catal. Commun*, 2022, **163**, 106414.
28. F. Cao, T. Wang and X. Ji, *Appl. Surf. Sci.*, 2019, **471**, 417-424.
29. B. Saravanakumara, G. Ravia, R. Yuvakkumara, V. Ganeshb and R. K. Guduru, *Mat. Sci. Semicon. Proc.*, 2019, **93**, 164-172.
30. C. Lin, X. Chen, L. Wang, W. Li, Z. Wang, M. Li, J. Feng, B. Hou and W. Yan, *Adv. Funct. Mater.*, 2024, 2401287.
31. J. Ding, L. Liu, J. Zhang, Y. Liu, H. Xu, Z. Shen, H. Yang, X. Feng, Y. Huang and B. Liu, *J. Am. Chem. Soc.*, 2025, **147**, 9601-9609.
32. H. Guo, W. Chen, X.-Q. Qiao, C. Li, B. Sun, D. Hou, M. Wang, X. W, T. Wuc, R. Chi and D.-S. Li, *Nano Energy*, 2025, **135**, 110672.
33. J. Ding, F. Li, J. Zhang, Q. Zhang, Y. Liu, W. Wang, W. Liu, B. Wang, J. Cai, X. Su, H. B. Yang, X. Yang, Y. Huang, Y. Zhai and B. Liu, *J. Am. Chem. Soc.*, 2023, **145**, 11829-11836.
34. Q. Dong, S. Ji, H. Wang, V. Linkov, R. Wang, *ACS Appl. Mater. Interfaces* 2022, **14**, 51222-51233.
35. U. Qamar, S. Roy, S. Kumar, B. Mukherjee, A. A. S. Devi, A. Goswami, P. Maiti and S. Das, *Adv. Funct. Mater.*, 2024, **34**, 2311943.
36. M. Zheng, P. Wang, X. Zhi, K. Yang, Y. Jiao, J. Duan, Y. Zheng and S.-Z. Qiao, *Am. Chem. Soc.*, 2022,**144**,14936-14944.
37. J. Ding, F. Li, X. Ren, Y. Liu, Y. Li, Z. Shen, T. Wang, W. Wang, Y. Wang, Y. Cui, H. Yang, T. Zhang and B. Liu, *Nat. Commun.*, 2024, **15**, 3641.
38. S. Qiao, G. Zhang, D. Tian, W. Xu, W. Jiang, Y. Cao, J. Qian, J. Zhang, Q. He and L. Song, *Energy Environ. Sci.*, 2024, **17**, 6779.
39. J.-Y. Kim, D. Hong1, J.-C. Lee, H. G. Kim, S. Lee, S. Shin, B. Kim, H. Lee, M. Kim, J. Oh, G.-D. Lee, D.-H. Nam and Y.-C. Joo, *Nat. Commun.*, 2021, **12**, 3765.
40. Z. Zhang, Q. Fang, X. Yang, S. Zuo, T. Cheng, Y. Yamauchi and J. Tang, *Adv. Mater.*, 2025, **37**, 2411498.
41. K. Poland, *J. solid state chem.* 1980, **31**, 145151.
42. V. Gajraj and C.R. Mariappan, *Appl. Surf. Sci.*, 2020, **512**, 145648.
43. J. Yan, J. Ni, H. Sun, C. Su and B. Liu, *Chinese J. Catal.*, 2024, **62**, 32-52.
44. H. Yang, C.-Q. Xu, S. Baskaran, Y.-R. Lu, C. Gu, W. Liu, J. Ding, J. Zhang, Q. Wang, W. Chen, J. Li, Y. Huang, T. Zhang and B. Liu, *EES Catal.*, 2023, **1**, 774.
45. W. Guo, S. Zhang, J. Zhang, H. Wu, Y. Ma, Y. Song, L. Cheng, L. Chang, G. Li, Y. Liu, G. Wei, L. Gan, M. Zhu, S. Xi, X. Wang, B. I. Yakobson, B. Z. Tang and R. Ye, *Nat. Commun.*, 2023, **14**, 7383.

46. Y. Huang, C. He, C. Cheng, S. Han, M. He, Y. Wang, N. Meng, B. Zhang, Q. Lu and Y. Yu, *Nat. Commun.*, 2023, **14**, 7368.
47. L. F. Shen, B. A. Lu, Y. Y. Li, J. Liu, Z. C. H. Fu, H. Peng, J. Y. Ye, X. M. Qu, J. M. Zhang, G. Li, W. B. Cai, Y. X. Jiang and S. G. Sun, *Angew. Chem., Int. Ed.*, 2020, **59**, 22397-22402.
48. Y. Yao, S. Zhu, H. Wang, H. Li and M. Shao, *Angew. Chem. Int. Ed.*, 2020, **132**, 10565-10569.
49. F. Lv, M. Sun, Y. Hu, J. Xu, W. Huang, N. Han, B. Huang and Y. Li, *Energy Environ. Sci.*, 2023, **16**, 201-209.
50. X. Chen, X.-T. Wang, J.-B. Le, S.-M. Li, X. Wang, Y.-J. Zhang, P. Radjenovic, Y. Zhao, Y.-H. Wang, X.-M. Lin, J.-C. Dong and J.-F. Li, *Nat. Commun.*, 2023, **14**, 5289.
51. L. F. Scatena, M. G. Brown and G. L. Richmond, *Science*, 2001, **292**, 908-912.
52. Y.-H. Wang, S. Zheng, W.-M. Yang, R.-Y. Zhou, Q.-F. He, P. Radjenovic, J.-C. Dong, S. Li, J. Zheng, Z.-L. Yang, G. Attard, F. Pan, Z.-Q. Tian and J.-F. Li, *Nature*, 2021, **600**, 81-85.
53. J. Ding, Z. Wei, F. Li, J. Zhang, Q. Zhang, J. Zhou, W. Wang, Y. Liu, Z. Zhang, X. Su, R. Yang, W. Liu, C. Su, H. B. Yang, Y. Huang, Y. Zhai and B. Liu, *Nat. Commun.*, 2023, **14**, 6550.
54. H. Niu, Z. Zhang, X. Wang, X. Wan, C. Kuai and Y. Guo, *Small*, 2021, **17**, 2102396.
55. J. Ding, L. Liu, J. Zhang, Y. Liu, H. Xu, Z. Shen, H. B. Yang, X. Feng, Y. Huang, B. Liu, *J. Am. Chem. Soc.*, 2025, **147**, 9601-9609.
56. Y. Wang, J. Ding, C. Su, Z. Shen, B. Liu, *Acc. Chem. Res.*, 2025, **58**, 2282-2295.
57. R. Zhang, Y. Guo, S. Zhang, D. Chen, Y. Zhao, Z. Huang, L. Ma, P. Li, Q. Yang, G. Liang and C. Zhi, *Adv. Energy Mater.*, 2022, **12**, 2103872.
58. H. Du, H. Guo, K. Wang, X. Du, B. A. Beshiwork, S. Sun, Y. Luo, Q. Liu, T. Li and X. Sun, *Angew. Chem. Int. Ed.*, 2023, **62**, e202215782.
59. J. Ma, Y. Zhang, B. Wang, Z. Jiang, Q. Zhang and S. Zhuo *ACS Nano*, 2023, **17**, 6687-6697.
60. W. Wen, P. Yan, W. Sun, Y. Zhou and X.-Y. Yu, *Adv. Funct. Mater.*, 2023, **33**, 2212236.
61. Y. Gao, K. Wang, C. Xu, H. Fang, H. Yu, H. Zhang, S. Li, C. Li and F. Huang, *Appl. Catal. B.*, 2023, **330**, 122627.
62. Q. Liu, L. Xie, J. Liang, Y. Ren, Y. Wang, L. Zhang, L. Yue, T. Li, Y. Luo, N. Li, B. Tang, Y. Liu, S. Gao, A. A. Alshehri, I. Shakir, P. O. Agboola, Q. Kong, Q. Wang, D. Ma and X. Sun, *Small*, 2022, **18**, 2106961.
63. Z. Li, J. Liang, Q. Liu, L. Xie, L. Zhang, Y. Ren, L. Yue, N. Li, B. Tang, A. A. Alshehri, M. S. Hamdy, Y. Luo, Q. Kong and X. Sun, *Mat. Today Phys.*, 2022, **23**, 100619.
64. Z. Li, Z. Deng, L. Ouyang, X. Fan, L. Zhang, S. Sun, Q. Liu, A. A. Alshehri, Y. Luo, Q. Kong and X. Sun, *Nano Res.*, 2022, **15**, 8914-8921.
65. S. Chen, G. Qi, R. Yin, Q. Liu, L. Feng, X. Feng, G. Hu, J. Luo, X. Liu and W. Liu, *Nanoscale*, 2023, **15**, 19577.
66. J. Yan, P. Liu, J. Li, H. Huang, S. Tong and W. Song, *Chem. Eng. J.*, 2024, **498**, 155108.
67. J. Yue, S. Liping, W. Yuechen, H. Lihua and Z. Hui, *Int. J. Hydrogen Energy*, 2024, **71**, 820-830.
68. J. Lv, Q.Yang, T. Liang, X. Sun, W. Rong, Q. Dai, Y. Gao, L. Wang, X. Xu, Y. Liu, *J. Am. Chem. Soc.*, 2025, **147**, 27708-27719.
69. J. Cai, Y. Wei, A. Cao, J. Huang, Z. Jiang, S. Lu, S.-Q. Zang, *Appl. Catal. B.*, 2022, **316**, 121683.